The following resources related to this article are available online at
www.sciencemag.org (this information is current as of April 7, 2009):

Updated information and services, including high-resolution figures, can be found in the online version of this article at:
http://www.sciencemag.org/cgi/content/full/323/5920/1503

Supporting Online Material can be found at:
http://www.sciencemag.org/cgi/content/full/1166467/DC1

A list of selected additional articles on the Science Web sites **related to this article** can be found at:
http://www.sciencemag.org/cgi/content/full/323/5920/1503#related-content

This article **cites 20 articles**, 8 of which can be accessed for free:
http://www.sciencemag.org/cgi/content/full/323/5920/1503#otherarticles

This article appears in the following **subject collections**:
Biochemistry
http://www.sciencemag.org/cgi/collection/biochem

Information about obtaining **reprints** of this article or about obtaining **permission to reproduce this article** in whole or in part can be found at:
http://www.sciencemag.org/about/permissions.dtl

the interaction was greatly enhanced in the presence of SYD-1 (Fig. 4, C, D, and G), suggesting that SYD-1 facilitates binding between ELKS-1 and SYD-2. Consistent with this result, SYD-1 directly interacted with ELKS-1 (Fig. 4, E and G), and this interaction was weakened in the presence of RSY-1ΔSR (Fig. 4, F and G). Thus, one way in which RSY-1 regulates SYD-2 function is indirectly by weakening the interaction of SYD-1 with ELKS-1 and thus potentially blocking the ability of SYD-1 to facilitate SYD-2 function (Fig. 4K).

Given that the ELKS-1/SYD-2 binding is very weak in the absence of SYD-1 in our assay, we could not test whether interaction of RSY-1 with SYD-2 inhibited ELKS-1/SYD-2 binding. However, the ELKS-1/SYD-2 interaction does increase when SYD-2 contains a gain-of-function mutation, $Arg^{184} \rightarrow Cys^{184}$ (R184C) (14), which was verified in our cell-based assay (Fig. 4, H and J). We then tested the effect of RSY-1 on this interaction and found that the interaction between ELKS-1 and SYD-2R184C was weakened in the presence of RSY-1ΔSR (Fig. 4, I and J), suggesting that, besides acting via SYD-1, RSY-1 can also directly antagonize the ability of SYD-2 to recruit ELKS-1 (Fig. 4K).

It is increasingly clear that positive and negative regulators control synapse development at multiple levels. For example, the transcription factor MEF2 globally regulates the number of excitatory synapses (7). Three ubiquitin ligase complexes also regulate presynaptic development (5, 8, 29). Here, RSY-1 was shown to act as a negative regulator of synaptogenesis by coun-

teracting SYD-1 function to inhibit SYD-2–dependent presynaptic assembly in the HSNL neuron. RSY-1 controls the amount of synaptic material recruited to presynaptic sites. RSY-1 also plays a role in establishing a balance between synapse formation and synapse elimination. RSY-1 achieves these functions by interacting with integral components of the synapse assembly machinery and by regulating a dense network of protein-protein interactions between various active-zone molecules (Fig. 4K).

References and Notes
1. M. Zhen, Y. Jin, *Nature* **401**, 371 (1999).
2. M. Zhen, Y. Jin, *Curr. Opin. Neurobiol.* **14**, 280 (2004).
3. C. L. Waites, A. M. Craig, C. C. Garner, *Annu. Rev. Neurosci.* **28**, 251 (2005).
4. Q. Chang, R. J. Balice-Gordon, *Neuron* **26**, 287 (2000).
5. P. van Roessel, D. A. Elliott, I. M. Robinson, A. Prokop, A. H. Brand, *Cell* **119**, 707 (2004).
6. K. Nakata et al., *Cell* **120**, 407 (2005).
7. S. W. Flavell et al., *Science* **311**, 1008 (2006).
8. M. Ding, D. Chao, G. Wang, K. Shen, *Science* **317**, 947 (2007); published online 11 July 2007 (10.1126/science.1145727).
9. M. P. Klassen, K. Shen, *Cell* **130**, 704 (2007).
10. V. Y. Poon, M. P. Klassen, K. Shen, *Nature* **455**, 669 (2008).
11. C. Desai, H. R. Horvitz, *Genetics* **121**, 703 (1989).
12. K. Shen, C. I. Bargmann, *Cell* **112**, 619 (2003).
13. M. R. Patel et al., *Nat. Neurosci.* **9**, 1488 (2006).
14. Y. Dai et al., *Nat. Neurosci.* **9**, 1479 (2006).
15. Materials and methods are available as supporting material on *Science* Online.
16. G. Zimowska et al., *Invest. Ophthalmol. Vis. Sci.* **44**, 4715 (2003).
17. P. Ouyang, *Biochem. Biophys. Res. Commun.* **263**, 192 (1999).
18. J. H. Joo et al., *Mol. Vis.* **11**, 133 (2005).
19. R. Alpatov et al., *Mol. Cell. Biol.* **24**, 10223 (2004).
20. P. Wang, P. J. Lou, S. Leu, P. Ouyang, *Biochem. Biophys. Res. Commun.* **294**, 448 (2002).
21. R. Baumeister, Y. Liu, G. Ruvkun, *Genes Dev.* **10**, 1395 (1996).
22. D. H. Hall, E. M. Hedgecock, *Cell* **65**, 837 (1991).
23. D. A. Wagh et al., *Neuron* **49**, 833 (2006).
24. R. J. Kittel et al., *Science* **312**, 1051 (2006); published online 13 April 2006 (10.1126/science.1126308).
25. S. L. Deken et al., *J. Neurosci.* **25**, 5975 (2005).
26. D. Blanchard, H. Hutter, J. Fleenor, A. Fire, *Mol. Cell. Proteomics* **5**, 2175 (2006).
27. M. D. Muzumdar, B. Tasic, K. Miyamichi, L. Li, L. Luo, *Genesis* **45**, 593 (2007).
28. J. Ko, M. Na, S. Kim, J. R. Lee, E. Kim, *J. Biol. Chem.* **278**, 42377 (2003).
29. T. A. Fulga, D. Van Vactor, *Neuron* **57**, 339 (2008).
30. We would like to thank the *Caenorhabditis* Genetics Center and the Japanese NBPR for strains; Y. Kohara (National Institute of Genetics, Japan) for Y53H1A.1 cDNAs; J. Audhya (University of California, San Diego) for *C. elegans* optimized mCherry cDNA; L. Luo (Stanford University) for vertebrate mCherry cDNA; T. Meyer (Stanford University) for eYFP-C3 plasmid; M. Park (Stanford University) for mCerulean-C1 plasmid; C. Gao for technical assistance; and members of the Shen lab, C. Bargmann, T. Clandinin, and L. Luo for critical comments on the manuscript. We would also like to thank B. Grill (Stanford University) for providing protocol and guidance for coimmunoprecipitation experiments. This work was funded by grants awarded to K.S. [from NIH (1R01NS048392), the Human Frontier Science Foundation, the Howard Hughes Medical Institute, and the W. M. Keck Foundation] and by a National Research Service Award predoctoral fellowship awarded to M.R.P. by NIH.

The Role of Fingerprints in the Coding of Tactile Information Probed with a Biomimetic Sensor

J. Scheibert,* S. Leurent, A. Prevost,† G. Debrégeas‡

In humans, the tactile perception of fine textures (spatial scale <200 micrometers) is mediated by skin vibrations generated as the finger scans the surface. To establish the relationship between texture characteristics and subcutaneous vibrations, a biomimetic tactile sensor has been designed whose dimensions match those of the fingertip. When the sensor surface is patterned with parallel ridges mimicking the fingerprints, the spectrum of vibrations elicited by randomly textured substrates is dominated by one frequency set by the ratio of the scanning speed to the interridge distance. For human touch, this frequency falls within the optimal range of sensitivity of Pacinian afferents, which mediate the coding of fine textures. Thus, fingerprints may perform spectral selection and amplification of tactile information that facilitate its processing by specific mechanoreceptors.

The hand is an important means for human interaction with the physical environment (1). Many of the tasks that the hand can undertake—such as precision grasping and manipulation of objects, detection of individual defects on smooth surfaces, and discrimination of textures—depend on the exquisite tactile sensi-

tivity of the fingertips. Tactile information is conveyed by populations of mechanosensitive afferent fibers innervating the distal fingerpads (2, 3). In recent years, a breakthrough in our understanding of the coding of roughness perception has been made with the experimental confirmation of Katz's historical proposition of the ex-

istence of two independent coding channels that are specific for the perception of coarse and fine textures (4–6). The perception of coarse textures (with features of lateral dimensions larger than about 200 μm) relies on spatial variations of the finger/substrate contact stress field and is mediated by the slowly adapting mechanoreceptors (7). The perception of finer textures (<200 μm) requires the finger to be scanned across the surface because it is based on the cutaneous vibrations thus elicited. These vibrations are intensively encoded, principally by Pacinian fibers (8), which are characterized by a band-pass behavior with a best frequency (i.e., the stimulus frequency where maximum sensitivity occurs) on the order of 250 Hz (9). The most elaborated description of the latter coding scheme was given by Bensmaïa and Hollins, who directly measured the skin vibrations of fingers scanning finely tex-

Laboratoire de Physique Statistique de l'Ecole Normale Supérieure, CNRS UMR 8550, Associé aux Universités Paris 6 et Paris 7, 24 rue Lhomond, 75231 Paris Cedex 05, France.

*Present address: Physics of Geological Processes, University of Oslo, Post Office Box 1048 Blindern, N-0316 Oslo, Norway.
†Present address: Laboratoire de Physique Théorique, 24 rue Lhomond, 75231 Paris Cedex 05, France.
‡To whom correspondence should be addressed. E-mail: georges.debregeas@lps.ens.fr.

tured substrates. They were able to correlate the perceived roughness of the surface with the power of the texture-induced vibrations weighted by the Pacinian spectral sensitivity (*10, 11*).

Among the four types of mechanoreceptors that convey tactile information, Pacinian corpuscles (PCs) have the most extended receptive field and therefore the lowest spatial resolution. This may seem paradoxical given their involvement in the tactile perception of fine features (*12, 13*). In standard psychophysical tests, the substrates used as stimuli are made of regularly spaced dots or bars (*1*). The resulting skin vibrations are confined to a single frequency whose value can be actively tuned by the subject through the scanning velocity so that it falls within the PC optimal range of sensitivity. Such regular stimuli substrates thus favor tactile identification or classification tasks. In contrast, for natural surfaces where features are randomly distributed and exhibit a wide spectrum of size, the elicited skin vibrations are expected to be spread over a large range of frequencies, among which only a limited fraction contributes to the PC activity.

To address this question on how low-resolution receptors encode fine textural information, the present study investigates the mechanical filtering properties of the skin. It aims at characterizing how textural information at any spatial scale (less than the finger/substrate contact diameter) is converted into subcutaneous vibrations in the vicinity of the mechanoreceptors during a dynamic tactile exploration. Because there is currently no way to measure experimentally the subcutaneous stress using a human subject, our approach is based on the use of a biomimetic tactile sensor whose functioning principle and main geometrical characteristics are matched to those of the human fingertip. This allows us to test, in particular, the role of epidermal ridges (fingerprints) in this transduction process. Two distinct functional roles have been so far attributed to these characteristic structures of the digital skin. Fingerprints are believed to reinforce friction and adhesion of the fingerpads, thus improving the ability to securely grasp objects or supports (*1, 14*). They may also be implicated in tactile perception, each of them acting as a magnifying lever, thus increasing the subsurface strain with respect to the surface deformation (*15, 16*). Here, we show that fingerprints may have a strong impact on the spectral filtering properties of the skin in dynamic tactile exploration.

The tactile sensor aims at mimicking the operation of the PC in dynamic tactile exploration (*17, 18*). As far as possible, the various geometrical and mechanical characteristics of the sensor are scaled to its biological counterpart (see fig. S1 for a comparison of key parameters). The sensing element consists of a microelectro mechanical system (MEMS) device that provides force measurements in a region of millimeter extension. This microforce sensor is attached to a rigid base and covered with an elastic spherical cap mimicking the fingertip skin (Fig. 1A). This

cap, made of cross-linked poly(dimethylsiloxane) (PDMS), has a maximum thickness $h = 2$ mm. Its surface is either "smooth" or "fingerprinted," that is, patterned with a regular square wave grating of period $\lambda = 220$ μm and depth 28 μm. The tactile sensor is mounted on a double cantilever system, allowing one to record the normal and tangential loads using capacitive position sensors. In a typical experiment, the sensor is scanned at constant velocity across a rigid, nom-

inally flat substrate under a constant normal load $P = 1.71$ N, yielding a contact zone of centimeter extension. This value for the load, together with the periodicity of the fingerprint-like structure, is chosen so that the number of ridges within the contact in the artificial system is close to that observed with an actual fingerpad under standard exploratory load (as illustrated in Fig. 1, B and C).

The stimuli consist of white-noise one-dimensional (1D) textured substrates (Fig. 1A,
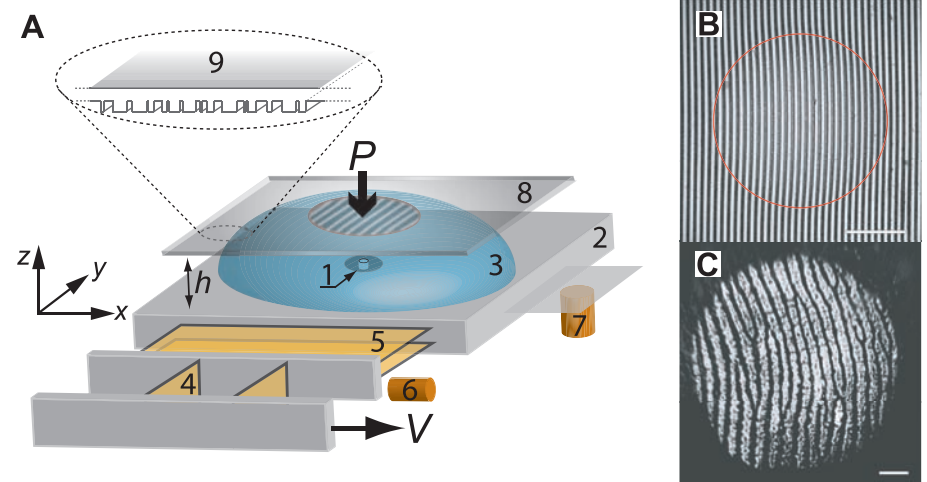
Fig. 1. (**A**) Sketch of the experimental setup. A MEMS microforce sensor (1) is mounted on a rigid base (2). It is covered with a spherical elastomer cap (3) of maximum thickness $h = 2$ mm and whose surface is smooth or patterned with parallel ridges. The resulting tactile sensor is mounted on a double-cantilever system (4, 5) allowing one to measure the total normal and tangential loads exerted on the sensor using capacitive position sensors (6, 7). In a typical experiment, the tactile sensor is scanned at constant speed v (using a linear motor) and under constant normal load P, across glass slides (8) whose surface is patterned with a 1D random square-wave grating (9). (**B**) Snapshot of the contact between the fingerprinted cap and a smooth glass slide in steady sliding. Wells between the elastomer's ridges appear bright, and the red circle, also shown on (A), defines the border of the contact. Actual contact only occurs on the ridges' summits. Ridges are slightly deformed at the periphery of the contact zone because of interfacial friction. (**C**) For comparison, this snapshot displays the contact between a human fingertip and a smooth glass surface with $P \approx 0.5$ N (a typical value in tactile exploration). Scale bars, 2 mm.

Fig. 2. (**A**) Typical pressure variation $p - \langle p \rangle$ measured with the smooth (blue) and fingerprinted (red) biomimetic fingers as a function of the substrate displacement u. The stimulus substrate used to produce these signals is a patterned glass slide exhibiting 1D random roughness. (**B**) Normalized power spectra of both signals obtained by Fourier transform averaged over four data sets, equivalent to a substrate of total length 180 mm. Shown in dashed lines is the theoretical power spectrum of the random pattern used as stimuli.
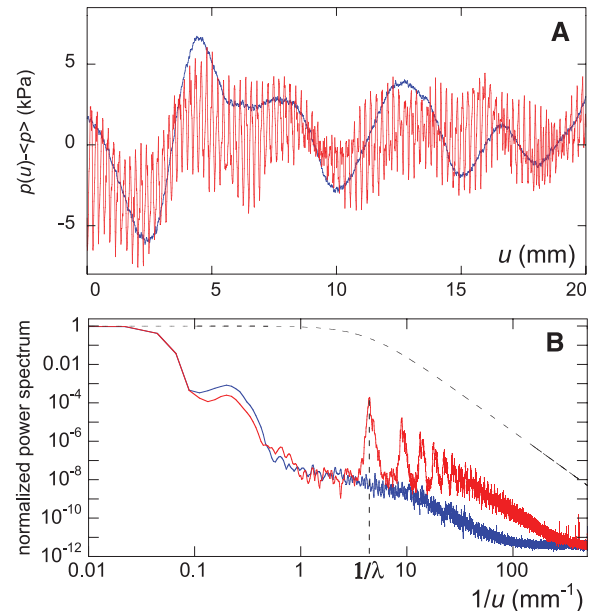
upper inset). They are obtained by patterning glass slides with a 28-μm-deep square wave grating whose edges are positioned at random positions with a mean grating width of 75 μm (17). The fingerprint-like ridges (when present) and substrate gratings are parallel to each other and oriented perpendicularly to the sliding direction. For moderate scanning velocities ($v < 0.4$ mm/s) and a given normal load, the pressure signal $p(t)$ is found to be a sole function of the substrate position at time t, regardless of the scanning velocity v (figs. S2 and S3). All experiments are performed at constant $v = 0.2$ mm/s, well within this velocity-independent regime of friction. To facilitate the analysis, data are systematically plotted as a function of the sensor/substrate relative displacement $u = vt$, as a strict equivalence exists between time and substrate displacement in steady sliding.

Figure 2A shows the typical pressure variations $p(u) - \langle p \rangle$ (where $\langle p \rangle$ is the average pressure) measured with the microforce device as the sensor is scanned across a textured surface. The smooth sensor exhibits pressure modulations with a characteristic wavelength in the millimeter range. The fingerprinted system reveals similar long-wavelength modulations to which are superimposed rapid oscillations whose period

corresponds to a displacement of the substrate over the interridge distance $\lambda = 220$ μm. A characterization of both sensors' filtering properties is given in Fig. 2B, which displays the power spectra of both signals together with that of the input stimulus, that is, the substrate topography (dashed line). The smooth sensor acts as a low-pass filter as it rapidly attenuates all pressure modulations induced by texture components of wavelength smaller than ≈ 1 mm. In contrast, the fingerprinted sensor exhibits band-pass filtering characteristics around the spatial frequency $1/\lambda$ (with further harmonics at integer multiples of $1/\lambda$). The presence of fingerprint-like ridges results in an amplification by a factor of 100 of the pressure modulations induced by a texture of wavelength λ (19).

These filtering characteristics can be interpreted to first order using a linear mechanical description of tactile sensing (20). Consider a small linear force sensor embedded at depth h in an elastic skin and located at ($x = 0, y = 0$). Its response to localized unit forces applied at various positions (x,y) on the skin surface defines its receptive field $F(x,y)$. The sensor signal p induced by any stress field $\sigma^s(x,y)$ applied at the skin surface then reads $p = \iint F(x, y)\sigma^s(x, y) dx\, dy$. We denote $\overline{\sigma}(x, y)$ the (time invariant)

contact stress field resulting from the continuous rubbing of a smooth substrate under a given load. If the substrate exhibits a fine texture, the stress field σ^s becomes dependent on the substrate position u. As u varies, σ^s is modulated around the reference field $\overline{\sigma}(x, y)$. The use of substrates exhibiting a two-level topography and a large enough contrast prevents any contact above the wells (as optically evidenced in fig. S4). The contact pressure is thus zero over half of the apparent contact region, whereas it is expected to be about twice the time-averaged stress field $\overline{\sigma}(x, y)$ at the location of the substrate summits. As a first approximation, one may thus write the superficial stress field as a function of u in the form

$$\sigma^s(x, y) = \overline{\sigma}(x, y).(1 + T(u - x)) \quad (1)$$

where $T(x)$ is the normalized two-level function ($T = \pm 1$), representing the topography of the surface. An exact calculation of the contact stress at a given location should take into account the local topography of the substrate and not just the average fraction of summits. The induced corrections should be important at short length-scales but become small when considering stress modulations over distances larger than the mean grating period.

With this expression, the pressure signal is then given by

$$p(u) = \langle p \rangle + \iint(F.\overline{\sigma})(x, y).T(u - x)dxdy \quad (2)$$

The transduction of tactile information is controlled by the product of the receptive field F and the reference stress field $\overline{\sigma}$. The function F characterizes the intrinsic properties of the receptor. It is expected to have a typical lateral extension of order h and to be fairly independent of the skin topography (such as fingerprints), provided that the height of the surface features is less than h (21). The reference field $\overline{\sigma}$ depends on the exploratory conditions such as the normal load P, the friction coefficient, or the position of the contact zone with respect to the sensor location. Unlike F, the stress field $\overline{\sigma}$ is highly sensitive to the skin surface topography. In particular, the presence of fingerprints a few tens of micrometers deep leads to a complete extinction of $\overline{\sigma}$ along regularly spaced lines (as illustrated in fig. S6), resulting in the observed spectral amplification of the signal at the frequency $1/\lambda$.

Equation 2 can be rewritten as $p(u) = \langle p \rangle + \int g_1(x)T(u - x)dx$ where $g_1(x) = \int (F.\overline{\sigma})(x, y)dy$ now defines the linear response function of the sensor with respect to 1D two-level stimuli substrates. The use of white-noise stimuli enables us to implement a Wiener-Volterra reverse-correlation method and extract $g_1(x)$ directly from the measurements, $g_1(x) = \langle p(u)T(u - x) \rangle$ (22, 23). The result of this computation for both smooth and fingerprinted sensors is plotted on Fig. 3. In qualitative agreement with the linear model, both response functions exhibit an

Fig. 3. Linearized stimulus-signal response functions $g_1(x)$ computed by cross-correlating the pressure signals and the stimulus topography $T(x)$, for both smooth (blue) and fingerprinted (red) systems. These data were obtained by averaging over three data sets, each one corresponding to a substrate length of 45 mm. The expected statistical deviation due to the finite length of the substrates was estimated numerically to be ±0.75 kPa/mm. This value is shown with the error bars and the shaded rectangle.
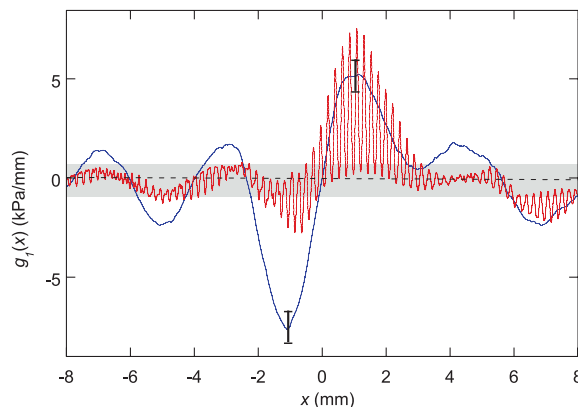
Fig. 4. (A) In red, pressure signal $p - \langle p \rangle$ measured with the fingerprinted sensor on a rough substrate. In blue, predicted signal obtained by convoluting the substrate topography function $T(x)$ with the linear response function $g_1(x)$. The latter was obtained independently by reverse correlation using two distinct 45-mm-long substrates. The dotted line indicates the $y = 0$ axis, and each interval along the y axis corresponds to a pressure variation of 1 kPa. For easier comparison, the same signals are plotted after applying **(B)** a low-pass filter with a cutoff frequency of $1/(2\lambda)$ and **(C)** a band-pass filter centered around the peak frequency $1/\lambda$.
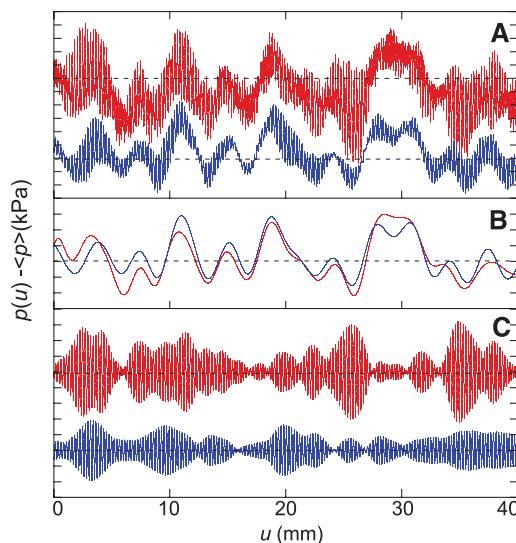
envelope of lateral extension of order h, and the response function of the fingerprinted sensor is further modulated with a spatial period λ. These functions can be tested by confronting actual measurements of $p(u) - \langle p \rangle$ with the predicted signal $\int g_1(x) T(u - x) dx$ as shown in Fig. 4A for the fingerprinted system. To facilitate the comparison, Fig. 4, B and C, displays the low- and high-frequency components, respectively. The linear response function allows one to reproduce the low-frequency signal. Although it correctly predicts the maxima and minima of the high-frequency component, it fails to capture its amplitude, which indicates that nonlinear effects might not be negligible for small length-scales. These effects could be taken into account by correlating p with the successive powers of T in order to include additional terms of the Wiener-Volterra series to describe the response function. However, this computation would require using a much larger set of stimuli to provide sufficient statistics.

Although the biomimetic tactile sensor used in this study offers a crude version of the finger physiology (24, 25), the mechanism of spectral selection it helped unravel depends on a very limited set of ingredients and should therefore be relevant to human digital touch. Namely, it requires that the surface of the tactile sensor displays a regularly ridged topography whose spatial period and amplitude are much smaller than the receptive field diameter and the mechanoreceptor's depth. In these conditions, such ridges have little influence on the skin deformations induced by a coarse texture (of spatial scale larger than the interridge distance λ). However, by shaping the interfacial contact stress field, such epidermal ridges give rise to an amplification of the subsurface stress modulations induced by a texture of characteristic wavelength equal to λ. In the time domain, this spatial period corresponds to a frequency $f_0 = v/\lambda$ where v is the finger/substrate relative velocity. In natural exploratory conditions, v is observed to be on the order of 10 to 15 cm/s (1). With a typical interridge distance $\lambda \approx 500$ μm, this yields a frequency $f_0 \approx 200$ to 300 Hz on the order of the best frequency of the Pacinian fibers that mediate the coding of fine textures. Fingerprints thus allow for a conditioning of the texture-induced mechanical signal that facilitates its processing by specific mechanoreceptors. It should be noted that this process is strongly dependent on the orientation of the ridges with respect to the scanning direction (fig. S7). In humans, fingerprints are organized in elliptical twirls so that each region of the fingertip (and thus each PC) can be ascribed with an optimal scanning orientation. Further studies are needed to elucidate how this may reflect on the exploratory procedures (such as fingertip trajectory and contacting zone) used by humans during texture evaluation tasks.

Remarkably, the response function of the fingerprinted system displayed in Fig. 3 is analogous to a Gabor filter because it provides both spatial and spectral resolution. Such filters are classically used in image analysis and have been identified in visual systems at the neural level (26). They are known to provide orientation discrimination, contrast enhancement, and motion detection. One may therefore expect, beyond the spectral filtering process discussed here, other interesting functional consequences of fingerprints, presumably relevant to the design of realistic haptic interfaces for humanoid robots (27, 28).

References and Notes

1. L. A. Jones, S. J. Lederman, *Human Hand Function* (Oxford Univ. Press, 2006).
2. I. Darian-Smith, in *Handbook of Physiology: The Nervous System: Sensory Processes* (American Physiological Society, Bethesda, MD, 1984), vol. 3, chap. 17.
3. K. O. Johnson, J. R. Phillips, *J. Neurophysiol.* **46**, 1177 (1981).
4. D. Katz, *The World of Touch*, I. E. Krueger, Transl. and Ed. (Hillsdale, NJ, Erlbaum, 1989; original work published 1925).
5. M. Hollins, S. J. Bensmaïa, S. Washburn, *Somatosens. Mot. Res.* **18**, 253 (2001).
6. M. Hollins, S. J. Bensmaïa, *Can. J. Exp. Psychol.* **61**, 184 (2007).
7. S. J. Lederman, M. M. Taylor, *Percept. Psychophys.* **12**, 401 (1972).
8. M. A. Srinivasan, J. M. Whitehouse, R. H. Lamotte, *J. Neurophysiol.* **63**, 1323 (1990).
9. J. C. Makous, R. M. Friedman, C. J. Vierck, *J. Neurosci.* **15**, 2808 (1995).
10. S. J. Bensmaia, M. Hollins, *Somatosens. Mot. Res.* **20**, 33 (2003).
11. S. J. Bensmaia, M. Hollins, *Percept. Psychophys.* **67**, 842 (2005).
12. R. S. Johansson, *J. Physiol.* **281**, 101 (1978).
13. M. Hollins, S. R. Risner, *Percept. Psychophys.* **62**, 695 (2000).
14. M. Cartmill, *Am. J. Phys. Anthropol.* **50**, 497 (1979).
15. N. Cauna, *Anat. Rec.* **119**, 449 (1954).
16. R. S. Fearing, J. M. Hollerbach, *Int. J. Robot. Res.* **4**, 40 (1985).
17. Materials and methods are available as supporting material on *Science* Online.
18. J. Scheibert, A. Prevost, J. Frelat, P. Rey, G. Debrégeas, *Europhys. Lett.* **83**, 34003 (2008).
19. A comparable spectral amplification is observed with finely abraded glass substrates (see fig. S5).
20. R. D. Howe, M. R. Cutkosky, *IEEE Trans. Robot. Autom.* **9**, 140 (1993).
21. K. L. Johnson, *Contact Mechanics* (Cambridge Univ. Press, Cambridge, 1985).
22. N. Wiener, *Nonlinear Problems in Random Theory* (MIT Press, Cambridge, MA, 1958).
23. F. Rieke, D. Warland, R. de Ruyter van Steveninck, W. Bialek, *Spikes: Exploring The Neural Code* (MIT Press, Cambridge, MA, 1999).
24. K. Dandekar, B. I. Raju, M. A. Srinivasan, *J. Biomed. Eng.* **125**, 682 (2003).
25. Q. Wang, V. Hayward, *J. Biomech.* **40**, 851 (2007).
26. J. P. Jones, L. A. Palmer, *J. Neurophysiol.* **58**, 1233 (1987).
27. R. Crowder, *Science* **312**, 1478 (2006).
28. V. Maheshwari, R. F. Saraf, *Science* **312**, 1501 (2006).
29. This project was supported primarily by CNRS basic funding and in part by the EU-NEST (New and Emerging Science and Technology) program, MONAT (Measurement of Naturalness) project (contract 21, number 29000). We are grateful to D. Chatenay and L. Bourdieu for fruitful discussions and careful reading of the manuscript.